Preprint Title Laser-processed antiadhesive bionic combs for handling of nanofibers inspired by nanostructures on the legs of cribellate spiders

Authors Sebastian Lifka, Kristóf Harsányi, Erich Baumgartner, Lukas Pichler, Dariya Baiko, Karsten Wasmuth, Johannes Heitz, Marco Meyer, Anna-Christin Joel, Jörn Bonse and Werner Baumgartner

Publication Date 05 Apr. 2022

Article Type Full Research Paper

Supporting Information File 1 Supplement to Laser-processed antiadhesive bionic combs for handling of nanofibers inspired by nanostructures on the legs of cribellate spiders.docx; 14.5 KB

ORCID® iDs Sebastian Lifka - https://orcid.org/0000-0002-7032-8373; Kristóf Harsányi - https://orcid.org/0000-0002-2015-2875; Dariya Baiko - https://orcid.org/0000-0001-7216-6665; Johannes Heitz - https://orcid.org/0000-0002-5608-5133; Marco Meyer - https://orcid.org/0000-0002-7527-7165; Anna-Christin Joel - https://orcid.org/0000-0002-7122-3047; Jörn Bonse - https://orcid.org/0000-0003-4984-3896

Laser-processed antiadhesive bionic combs for handling of nanofibers inspired by nanostructures on the legs of cribellate spiders.

Sebastian Lifka[1,*], Kristóf Harsányi[1], Erich Baumgartner[1], Lukas Pichler[1], Dariya Baiko[1], Karsten Wasmuth[4], Johannes Heitz[2], Marco Meyer[3], Anna-Christin Joel[3], Jörn Bonse[4] and Werner Baumgartner[1]

Address:

[1]Institute of Biomedical Mechatronics, Johannes Kepler University Linz, Altenberger Straße 69, 4040 Linz, Austria

[2]Institute of Applied Physics, Johannes Kepler University Linz, Altenberger Straße 69, 4040 Linz, Austria

[3]Institute of Biology II (Zoology), RWTH Aachen University, Worringerweg 3, 52074 Aachen, Germany

[4]Bundesanstalt für Materialforschung und –prüfung (BAM), Unter den Eichen 87 12205 Berlin, Germany

Email: Sebastian Lifka – sebastian.lifka@jku.at

* Corresponding author

Abstract

Nanofibers are drawing the attention of engineers and scientists because their large surface-to-volume ratio is favorable for applications in medicine, filter technology,

textile industry, use in lithium-air batteries and in optical sensors. However, when transferring nanofibers to a technical product in the form of a random network of fibers, referred to as non-woven fabric, the stickiness of the freshly produced and thus fragile nanofiber non-woven remains a problem. This is mainly because nanofibers strongly adhere to any surface because of van der Waals forces. In nature, there are animals that are actually able to efficiently produce, process, and handle nanofibers: cribellate spiders. For that, the spiders use the calamistrum, a comb-like structure of modified setae on the metatarsus of the hindmost (fourth) legs, to which the 10 – 30 nm thick silk nanofibers do not stick due to a special fingerprint-like surface nanostructure. In this work, we present a theoretical model of the interaction of linear nanofibers with a sinusoidal corrugated surface. This model allows a prediction of the adhesive interaction and, thus, the design of a suitable surface structure to prevent sticking of an artificially non-woven of nanofibers. According to the theoretical prediction, a technical analogon of the nanoripples was produced by ultrashort pulse laser processing on different technically relevant metal surfaces in the form of so-called laser-induced periodic surface structures (LIPSS). Subsequently, by means of a newly established peel-off test, the adhesion of an electrospun polyamide fiber-based non-woven was quantified on such LIPSS-covered titanium-alloy and steel samples, as well as on polished (flat) control samples as reference. The latter revealed that the adhesion of electrospun nanofiber non-woven is significantly lowered on the nanostructured surfaces than on the polished surfaces.

Keywords

biomimetics, electrospinning, laser-induced periodic surface structures (LIPSS), nanofibers, nanostructures

Introduction

Nanofibers have a diameter of approximately 10 to 800 nanometers, whereas their length is much greater compared to their diameter, which is why the term fiber or thread is used. These are constantly drawing the attention of engineers because their surface-to-volume ratio is favorable for applications in medicine, filter technology, textile industry, use in lithium-air batteries and optical sensors. [1−7]

The inherently small scale makes production as well as further processing of nanofibers challenging [8]. For the technical production of artificial nanofibers different methods like electrospinning [1-2, 6-8] or microfluidic spinning [4] are established. Despite a lot of effort to facilitate the production and handling of nanofibers [3−7] the stickiness of freshly produced and thus fragile nanofiber non-woven mats remains a problem. This is mainly because nanofibers strongly adhere to any surface due to van der Waals forces [9]. This force, named after the Dutch physicist Johannes Diderik van der Waals, is the temporal averaging from the interaction of constantly moving and interacting positive and negative charges (dipoles) in matter and the briefly occurring electric and magnetic fields. These varying electric fields occur not only because of thermal motion of electric charges, but also because of the quantum mechanical fuzziness of their location or moment. The more charges there are at a specific location, the greater the force, because more interactions occur. For this reason, the van der Waals force, which is also called the charge fluctuation force, between two bodies is strongly dependent on the distance *d* between the two bodies [9]. For a cylindrical fiber with radius *R* interacting with the plane surface of a semi-infinite body the energy per unit length due to van der Waals interaction is given as [10]

$$\mu = \lim_{R1\to\infty}(G) = -\sqrt{2R}\cdot\frac{A_H}{24d^{3/2}} \qquad (1)$$

with the Hamaker-constant A_H that is according to [9]

$$A_H = \pi^2 \cdot \rho_1 \cdot \rho_2 \cdot c. \quad (2)$$

Here, the mass densities (ρ_1, ρ_2) of the interacting bodies and the London coefficient *c*, which describes the particle-particle interaction, are multiplied.

The van der Waals energy U_{vdW} of the fiber obtained due to the interaction is the integral of the above interaction function μ over the entire fiber length *l*, which can depend on the position along the fiber:

$$U_{vdW} = \int_l \mu\,(l) dl. \quad (3)$$

This formulation could be interpreted in such a way that if the radius of the fiber decreases, the van der Waals force also decreases and can, therefore, be neglected if *R* is sufficiently small. However, this is not always the case because:

1. Due to the smaller radius, the fiber also becomes softer and thus the easier deflection can increase the contact area resulting in larger forces. The van der Waals force is proportional to the root of the radius, $\mu \sim \sqrt{R}$, and the materials stiffness, expressed by the area moment of inertia *J* is proportional to the radius to the fourth power, $J \sim R^4$. Hence, the fiber gains more contact area much faster than the force decreases.

2. With a smaller radius, more fibers can attach simultaneously to the surface, which leads to a further increase in the total interacting surface area.

Though technical nanofiber handling and processing is limited today, in nature, there are animals that are actually able to efficiently produce, process, and handle nanofibers: cribellate spiders [11, 12]. Their capture thread consists of one or two axial fibers as “construction elements”, surrounded by a wool of nanofibers. This wool is

used to capture prey, deploying van der Waals forces and additionally embedding the fibers into the viscous waxy layer of the insects' cuticle [13, 14]. One thread typically consists of 5000 to 30000 single fibers with a thickness of 10 − 30 nm. In the spinning process, the spiders extract this silk from the cribellum (spinning plate) and process it by "combing" the fibers to form a puffy structure surrounding the axial fibers [11]. To process the fibers, the spiders use the calamistrum, a comb-like structure of modified setae on the metatarsus of the hindmost (fourth) legs [11] (Figure 1). The 10 – 30 nm thick silk nanofibers do not stick to the calamistrum due to a special fingerprint-like nanostructure. This was characterized recently [10] for the calamistrum of *Uloborus plumipes* (commonly named feather-legged lace weaver or the garden center spider). Its fingerprint-like outmost surface structure builds an approx. sinusoidal cross-section with a periodicity of approx. 200 – 300 nm and a height (amplitude) of approx. 200 nm. During the combing process, the nanofibers are pulled orthogonally over these nanoripples. It was shown that the nanostructure on the calamistrum in fact reduces adhesion of native spider silk and this reduced adhesion can be mimicked by artificially structured polymer foils [10].

In order to technically integrate these antiadhesive structures, the structures have to be adapted as typical technical nanofibers differ in diameter and material properties (like the Young's modulus (elastic modulus)) quite significantly from spider silk fibers.

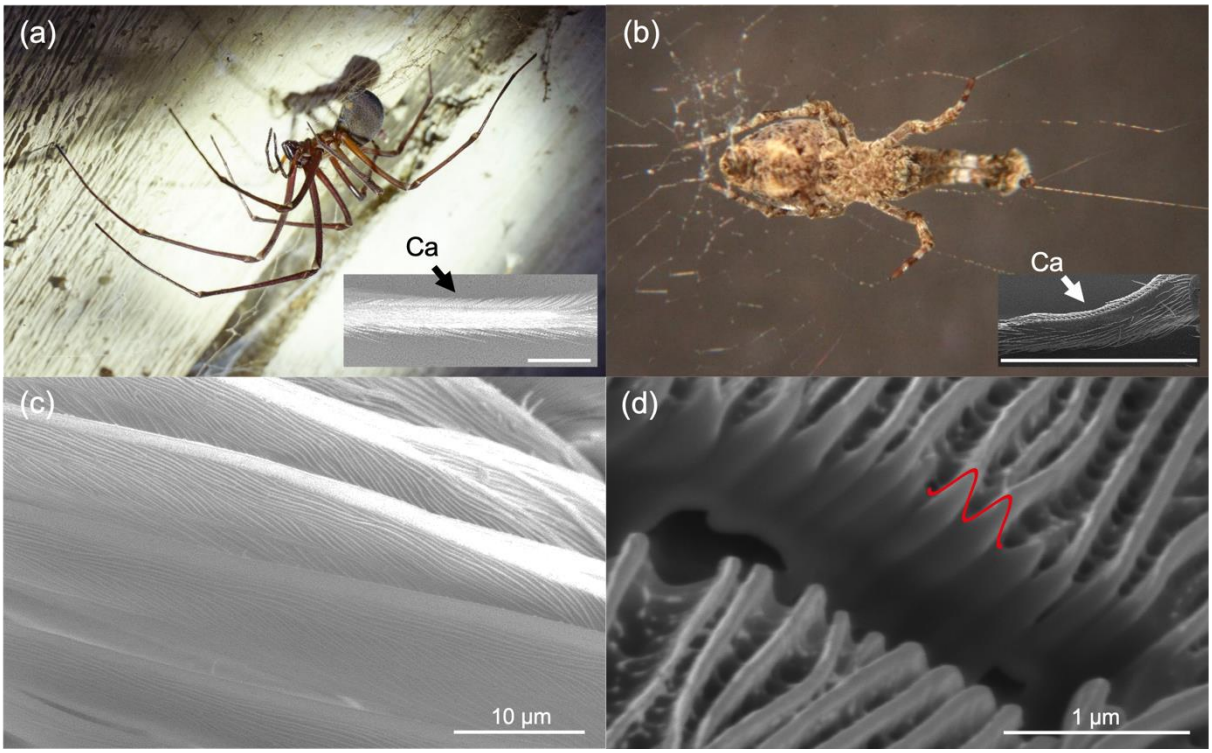

Figure 1: Images of four distantly related and differently sized cribellate spiders with same-sized nanoripples covering their calamistrum (antiadhesive comb to handle nanofibers). (a) Photography of the endemic and last species of an old Gondwanan lineage, the Tasmanian cave spider *Hickmania troglodytes* (body size of up to 2 cm [15] and a leg span up to 18 cm [16]). (b) Photography of the cosmopolitan feather-legged lace weaver *Uloborus plumipes* (body size up to 0.6 cm [17]). (c) Scanning electron micrograph of the calamistrum of *Jamberoo johnnoblei* (body size up to 0.8 cm [18]). (d) FIB-cut high resolution SEM image through the nanoripples on the calamistrum of the lace-webbed spider *Amaurobius similis* (body size up to 1.2 cm [19]), highlighting in red the abstracted sinusoidal surface corrugation as cross-sectional profile of the nanoripples. The insets in (a) and (b) provide SEM micrographs of the calamistra (Ca) of the respective spiders, with scale bars of 0.8 mm length. Data is presented in Table S1 in the supporting information file 1.

In this work, we present a theoretical model of the interaction of nanofibers with a sinusoidal surface based on an energy approach. This model allows a prediction of the adhesive interaction and thus the design of a suitable surface structure to prevent sticking of an artificially non-woven of nanofibers. Similar to the *Lotus effect* [20 - 23] where the wettability of the hierarchical surface structure of the lotus leaf can be described with an energy approach related to the surface free energy of the fluid, here we use an energy approach related to the bending energy of the nanofibers to describe the fiber adhesion on structured surfaces.

Laser-induced periodic surface structures (LIPSS) [24] represent a technical analogon of the nanoripples found on the calamistrum of the spider. They were produced by ultrashort pulse laser processing on different technically relevant metal (titanium-alloy and steel) surfaces according to the theoretical prediction. Subsequently, the adhesion of electrospun polyamide fibers was quantified on these structures as well as on polished (flat) control samples as reference. This bioinspired laser-based surface functionalization paves a new way for technologically improving the production of tools for handling of artificial nanofibers that can facilitate and optimize the production of filter materials, nanofabrics, and further more.

Results and Discussion

Theoretical modelling

The general model is depicted in Figure 2. The course of the fiber is divided into two areas along the length coordinate x: 1. the contact area, i.e. the area between the contact points (marked by red full circles in Figure 2), where the fiber adheres to the surface, and 2. the sagging area, where the fiber has no contact to the surface. The point of detachment of the fiber from the surface is defined as the detachment point x_0.

This point can parametrize the curve and is initially assumed to be known. The fiber is assumed to have a certain bending stiffness and, thus, it can be modelled according to the linear elastic (Hookean) beam theory (Euler-Bernoulli-beam-theory). Thus, we have to solve the ordinary differential equation (ODE) [25]

$$w''(x) = \frac{-M}{EJ}, \tag{4}$$

with w describing the deflection from neutral position, M denoting the bending moment, E describing the Young's elastic modulus and J denoting the second moment of area (moment of inertia of plane area).

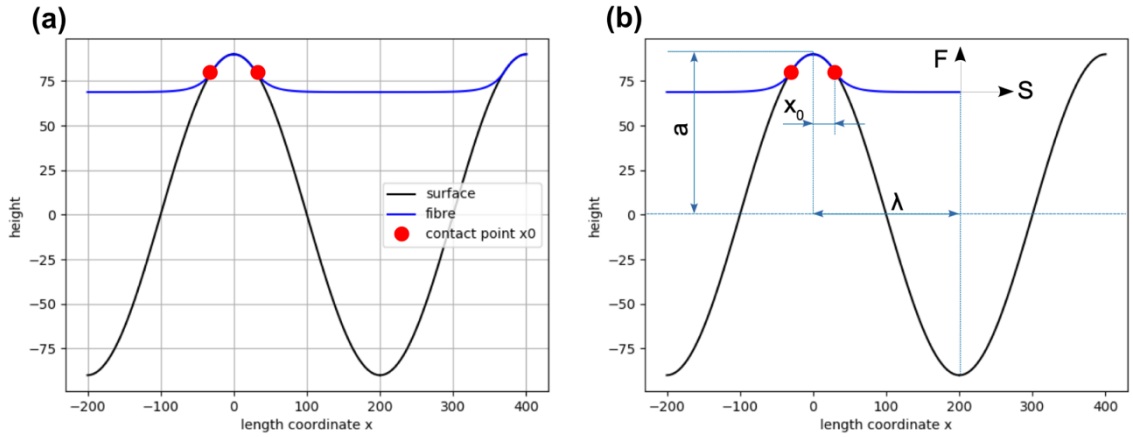

Figure 2: Principle geometry of the interaction of a nanofiber with a periodic sinusoidal surface topography (a) and as single length unit when cut free (b). The periodic surface structure is drawn in black, and the fiber in blue color and mathematically modelled by functions $f(x)$ and $w(x)$, respectively. The cross-section of the surface is sinusoidal with a period of 2λ and an amplitude of a. A fiber on top of the surface is deflected partially due to van der Waals interactions. The point of detachment x_0 is used as parameter to characterize the system. A longitudinal force S can stretch the fiber. For theoretical modelling, a single unit is cut free (b) and the action of the fiber at $x > \lambda$ is replaced by the yet unknown vertical force F. This force needs to enforce the slope of the fiber at $x = \lambda$ to be zero.

In order to solve the above ODE we need to know the bending moment and adequate boundary conditions. According to the model depicted in Figure 2 we assume to precisely know the position of the point of detachment x_0. At this location the two boundary conditions are

$$w(x_0) = f(x_0) \text{ and}$$
$$w'(x_0) = f'(x_0)\,, \tag{5}$$

i.e. the mathematical curve describing the fiber $w(x)$ touches the curve describing the surface profile $f(x)$. To get the bending moment, we cut the fiber virtually at position λ, i.e. in the middle of one period of the periodic surface structure. We know that a longitudinal force S is applied to the fiber in natural as well as in technical nanofiber production, and we assume a force F acting vertical at the cutting-position position λ to bring the system back into equilibrium. This force is used to enforce the slope $w'(\lambda)$ to be zero, i.e. there is a horizontal tangent and, thus, $w'(x)$ is continuous and continuous differentiable at position λ. Hence, the ODE in Eq. (4) can be solved by generally assuming a force F and calculate F according to the demand that $w'(\lambda) = 0$.

The general solution of Eq. (4) can be written as

$$w(x) = \frac{F\cdot\lambda}{S} - \frac{F\cdot x}{S} + w(\lambda) + C_1 \cdot exp\left[\sqrt{\frac{S}{EJ}}\cdot(x-\lambda)\right] + C_2 \cdot exp^{-1}\left[\sqrt{\frac{S}{EJ}}\cdot(x-\lambda)\right]. \tag{6}$$

For the following, this can be simplified as at position $x = \lambda$ Eq. (6) becomes

$$w(\lambda) = C_1 + C_2 + w(\lambda). \tag{7}$$

Thus, we obtain directly

$$C_1 = -C_2 \overset{\text{def}}{=} C. \tag{8}$$

Substituting Eq. (8) into Eq. (6) and performing a derivation with respect to *x* we obtain *w'*(*x*) as

$$w'(x) = \frac{F}{S} + C \cdot \sqrt{\frac{S}{EJ}} \left\{ exp\left[\sqrt{\frac{S}{EJ}} \cdot (x - \lambda) \right] - exp^{-1}\left[\sqrt{\frac{S}{EJ}} \cdot (x - \lambda) \right] \right\}. \quad (9)$$

In order to obtain $w'(\lambda) = 0$ we can insert $x = \lambda$ in Eq. (9) yielding

$$w'(\lambda) = \frac{-F}{S} + C \cdot \sqrt{\frac{S}{EJ}} \cdot 2 = 0 \Rightarrow F = 2S \cdot C \cdot \sqrt{\frac{S}{EJ}}. \quad (10)$$

Insertion of Eq. (10) into Eq. (6) and using the definition of the hyperbolic sine we obtain

$$w(x) = 2C \cdot \left[sinh\left(\sqrt{\frac{S}{EJ}} \cdot (x - \lambda) \right) \cdot (x - \lambda) \right] + w(\lambda). \quad (11)$$

Now, to fulfil the second part of Eq. (5) we have to differentiate Eq. (11) and solve the equation so that $w'(x=x_0) = f'(x=x_0)$.

$$w'(x_0) = 2C \cdot \left[\sqrt{\frac{S}{EJ}} \cdot cosh\left(\sqrt{\frac{S}{EJ}} \cdot (x_0 - \lambda) \right) \right] - \sqrt{\frac{S}{EJ}} \stackrel{\text{def}}{=} f'(x_0) \quad (12)$$

This directly yields

$$C = \frac{f'(x_0)}{2 \cdot \sqrt{\frac{S}{EJ}} cosh\left(\sqrt{\frac{S}{EJ}} (x_0 - \lambda) \right)}. \quad (13)$$

Finally, in order to fulfil the boundary conditions $w(x=x_0) = f(x=x_0)$ one has to calculate $w(\lambda)$ which can be obtained to be

$$w(\lambda) = f(x_0) - C \cdot \left[sinh\left(\sqrt{\frac{S}{EJ}} \cdot (x_0 - \lambda) \right) - \sqrt{\frac{S}{EJ}} \cdot (x_0 - \lambda) \right]. \quad (14)$$

Taken together, if the topography function of the surface structure $f(x)$ is given the bending line which only depends on the position of the contact point x_0 is given to be

$$w(x) = 2C \cdot \left[sinh\left(\sqrt{\frac{S}{EJ}} \cdot (x - \lambda) \right) \cdot (x - \lambda) \right] + w(\lambda)$$

with $C = \frac{f'(x_0)}{2 \cdot \sqrt{\frac{S}{EJ}} cosh\left(\sqrt{\frac{S}{EJ}} (x_0 - \lambda) \right)}$ (15)

and $w(\lambda) = f(x_0) - C \cdot \left[sinh\left(\sqrt{\frac{S}{EJ}} \cdot (x_0 - \lambda) \right) - \sqrt{\frac{S}{EJ}} \cdot (x_0 - \lambda) \right]$.

A special case should be considered separately, namely if $S = 0$, i.e. if no longitudinal force is applied and the fiber can freely form contact with the surface. Instead of reformulating the above result using del Hospital's rule, we could simply solve the initial differential equation (4) with $S = 0$, which directly leads to

$$w(x) = f(x_0) + \frac{F}{EJ} \cdot \left(\frac{x_0^3}{3} - \frac{x \cdot x_0^2}{2} - \frac{\lambda \cdot x_0^2}{2} + \frac{\lambda \cdot x \cdot x_0}{1} - \frac{\lambda \cdot x^2}{2} + \frac{x^3}{6} \right) + f'(x_0) \cdot (x - x_0). \quad (16)$$

When now F is adjusted so that $w'(\lambda) = 0$ we obtain for this special case without longitudinal force

$$w(x) = f(x_0) - f'(x_0) \cdot \frac{x_0^2 + (3 \cdot \lambda - x) \cdot x_0 + 2 \cdot x^2 - 3 \cdot \lambda \cdot x}{3 \cdot (x_0 + x + 2 \cdot \lambda)}. \quad (17)$$

Now, in any case the position x_0 of the contact point remains to be determined. For this, we need to find the energy-minimum of the system with respect to x_0, which would correspond to the position where in equilibrium the fiber detaches from the surface structure. There are three energetic contributions to the energy of the whole system that depend on x_0:

i) The bending energy of a fiber in contact with the surface, i.e. the elastic energy stored in the fiber in the region of contact from $x = 0 \ldots x_0$, which can be calculated for a linear elastic beam as

$$E_1(x_0) = \frac{EJ}{2} \cdot \int_0^{x_0} w''(x)^2 \, dx = \frac{EJ}{2} \cdot \int_0^{x_0} f''(x)^2 \, dx. \quad (18)$$

ii) The bending energy of the free fiber, i.e. in the region of no contact from $x = x_0 \ldots \lambda$, which follows to be

$$E_2(x_0) = \frac{EJ}{2} \cdot \int_{x_0}^{\lambda} w''(x)^2 \, dx. \tag{19}$$

iii) Finally, the van der Waals energy which according to Eq. (3) follows to be

$$E_3(x_0) = -\int_0^{x_0} \mu(x) \cdot \sqrt{1 + w'(x)^2} dx. \tag{20}$$

It must be emphasized that in principle the above term can also account for other (additional) attractive energies like electrostatic interactions. All these can be summarized in the $\mu(x)$ and can, therefore, depend on the position and thereby on the distance of fiber and surface ($w(x)$ - $f(x)$).

However, only the van der Waals energy E_3 exhibits a negative sign and thus decreases the total energy stored in the system, leading to more deflection and thus to more contact of the fiber with the surface. In contrast, the elastic energies E_1 and E_2 increase the total energy

$$E_{tot}(x_0) = E_1(x_0) + E_2(x_0) + E_3(x_0). \tag{21}$$

In order to find the fiber detachment point x_0 in the equilibrium, one needs to solve the optimization problem

$$\frac{\partial E_{tot}}{\partial x_0} = 0. \tag{22}$$

A general analytical solution to this optimization problem for any surface, i.e. for any $f(x)$, cannot be found. However, numerical solutions are easily possible and for some cases even approximate analytical solutions are available. Let us assume the surface to be described by a cosine function, i.e.

$$f(x) = a \cdot cos\left(\frac{x \cdot \lambda}{\pi}\right). \tag{23}$$

It has to be emphasized that if the periodic modulation on the surface has a sinusoidal cross-section but the fiber is not orthogonally oriented to these ridges, the cross-section under an angle is still represented by a cosine function with same amplitude *a* but another characteristic length *λ*. Thus, the formal description derived here is still valid.

Due to the high exponent of the dependence of van der Waals energy and distance we can approximate the system and assume that we have a constant $\mu = \mu_{vdW}$ from $x = 0...x_0$ and $\mu = 0$ from $x = x_0 \ldots \lambda$. For this, we obtain the energy contributions in the case of finite longitudinal force *S* as

$$E_1(x_0) = \frac{\pi^3 \cdot EJ \cdot a^2 \cdot \left(\lambda \cdot sin\left(\frac{2 \cdot \pi \cdot x_0}{\lambda}\right) + 2 \cdot \pi \cdot x_0\right)}{8 \cdot \lambda^4},$$

$$E_2(x_0) = \int_{x_0}^{\lambda} \left(\frac{\left(\pi \cdot S \cdot a \cdot sinh\left(\sqrt{(S/EJ)} \cdot (x - \lambda)\right) \cdot sin((\pi \cdot x_0)/\lambda)\right)}{EJ \cdot \sqrt{(S/EJ)} \cdot \lambda \cdot \left(cosh\left(\sqrt{(S/EJ)} \cdot (x_0 - \lambda)\right) - 1\right)} \right)^2 dx$$

$$\left[\frac{\pi \cdot a}{\lambda} \cdot sin\left(\frac{\pi \cdot x_0}{\lambda}\right)\right]^2 \cdot \frac{S}{16} \cdot \left[cosh\left(\sqrt{\frac{S}{EJ}} \cdot (x_0 - \lambda)\right)\right]^{-1} \cdot \tag{24}$$

$$\left[\sqrt{\frac{EJ}{S}} \cdot e^{-2 \cdot \sqrt{S/EJ} \cdot (x_0 + \lambda)} \cdot \left(e^{4\sqrt{\frac{S}{EJ}} \cdot x_0} - e^{4\sqrt{\frac{S}{EJ}} \cdot \lambda} - 4\pi^2 \sqrt{\frac{S}{EJ}} \cdot e^{2\sqrt{\frac{S}{EJ}} \cdot (x_0 + \lambda)}\right) - 4\lambda\right],$$

$$E_3(x_0) = -\mu_{vdW} \cdot \int_0^{x_0} \sqrt{1 + \frac{\pi^2 \cdot a^2}{\lambda^2} \cdot sin\left(\frac{\pi \cdot x}{\lambda}\right)^2}\, dx.$$

The integral for E_3 can be solved using complex incomplete elliptic integrals of the second kind. These can be calculated numerically. The system tends to the state of minimal total energy, therefore to a state where $E_1 + E_2 + E_3 \rightarrow min$.

In principle, there are three possible states:

A) It requires more energy to bend the fiber to adapt to the surface than can be gained due to van der Waals interaction. A straight fiber touches only the tips of the surface.

B) It is energetically favorable to deflect the fiber in order to obtain the interaction energy, but not all to the bottom of the sinusoidal surface topography. Thus, a clear total energy minimum exists.

C) Bending requires less energy than can be gained by the van der Waals interaction. Thus, the fiber adapts completely to the shape of the surface.

The energies and the corresponding shape of the fiber-adaption to the surface of these three possible states, when the elastic modulus is assumed E = 80 MPa (a typical value for spider silk [26]) and S = 0 N, are shown in Figure 3. Figure 3(a) and 3(b) show state A, Figure 3(c) and 3(d) show state B and Figure 3(e) and 3(f) show state C.

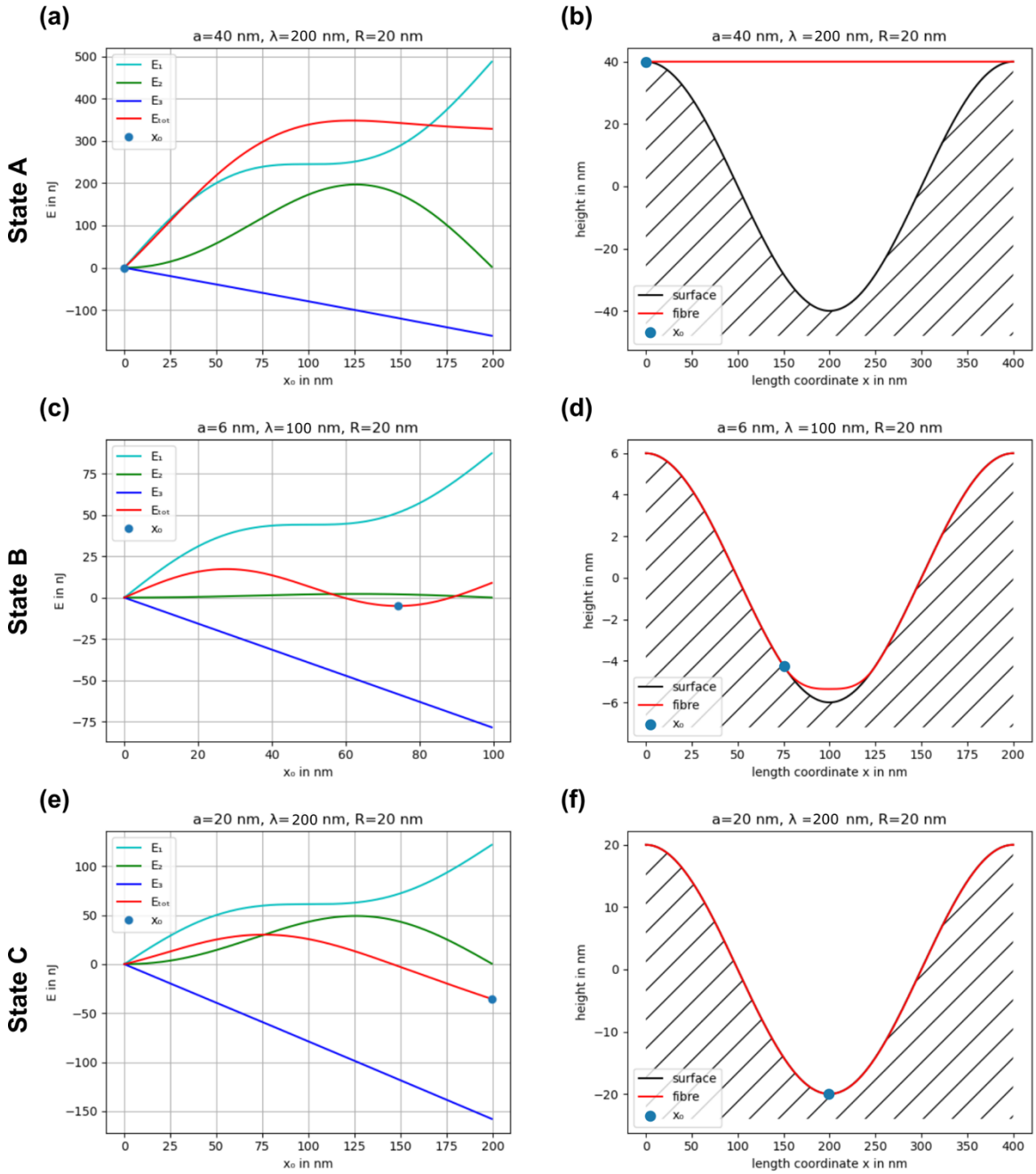

Figure 3: The three possible states: A (a, b), B (c, d) and C (e, f). (a, c, e) show the total energies E_{tot} dependent on the parameter x_0. (b, d, f) show the corresponding energetically most favorable shape of the fiber-adaption to the surface. The blue full circles mark that x_0 at which E_{tot} is minimal and, thus, the point where the fiber detaches from the surface. The elastic modulus is assumed E = 80 MPa and S = 0 N. a denotes the amplitude, λ denotes the half of the period of the sinusoidal surface cross section and R is the fiber radius.

State B only exists in a very narrow parameter window and, thus, can be neglected. We were able to find a solution for the transition out of state C, in the following also called the adhesive state, into an anti-adhesive state, in dependence on only a few parameters and some constants like the Hamaker-constant and the elastic modulus of the fiber. These free parameters are the amplitude *a* and the spatial period $\Lambda = 2\lambda$ of the sinusoidal surface as well as the bending stiffness and thus of the radius of the fiber in the case of $S = 0$.

While finding the minimum of the energy is cumbersome when trying to find an analytical solution, the slope of the total energy can be calculated as

$$\frac{\partial(E_1+E_2+E_3)}{\partial x_0}\Big|_{x_0=0} = \frac{\pi^4 \cdot EJ \cdot a^2}{2 \cdot \lambda^4} - \mu. \tag{25}$$

Thus, if

$$a \leqslant \sqrt{\frac{2 \cdot \lambda^4 \cdot \mu}{\pi^4 \cdot EJ}} \tag{26}$$

the fiber will adhere well as the energy directly decreases from $x_0 = 0$. For $E = 80$ MPa, a Hamaker-constant $A_H = 7.5 * 10^{-2}$ and for different fiber radii *R* (in nm) the results are shown in Figure 4.

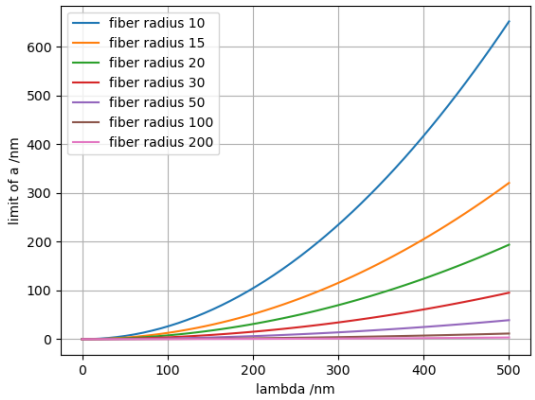

Figure 4: Transition from adhesive to anti-adhesive state for varying fiber radii ranging between 10 nm and 200 nm. The individual curves represent a lower limit of the surface modulation amplitude *a*, i.e. the surface is adhesive through van der Waals forces only for values below the corresponding curves.

Design and test of LIPSS-covered metal surfaces that are anti-adhesive for electrospun PA-6 fibers

In order to test the theory derived above, electrospinning of polyamide 6 (PA-6) in a laboratory setup onto structured metal samples (titanium-alloy and steel) was performed and the peel-off-forces were determined using a custom made peel-test device. PA-6 has an elastic modulus E of 0.6 up to 2.5 GPa, dependent on the treatment and the environmental conditions [27]. With our custom made electrospinning setup the typical diameters of the fibers are > 140 nm. Thus, from Eq. (26) we can follow that adhesion is impaired if the modulation depth (amplitude) a > 250 nm when assuming E = 1 GPa, R = 70 nm and an average in-surface-plane inclination angle of the fiber of 45° with respect to the ripple ridge direction. The angle is used to take statistically into account that the fibers will orient randomly on the surface, i.e. the fibers form a kind of mesh on the surface ripples, as can be seen in

Figure 5. Thus, not all will orient perpendicular to the surface ripples. The modulation depth that typically can be achieved for LIPSS (LSFL type [28]) on metals is up to 400 nm. Thus, an antiadhesive effect can be assumed.

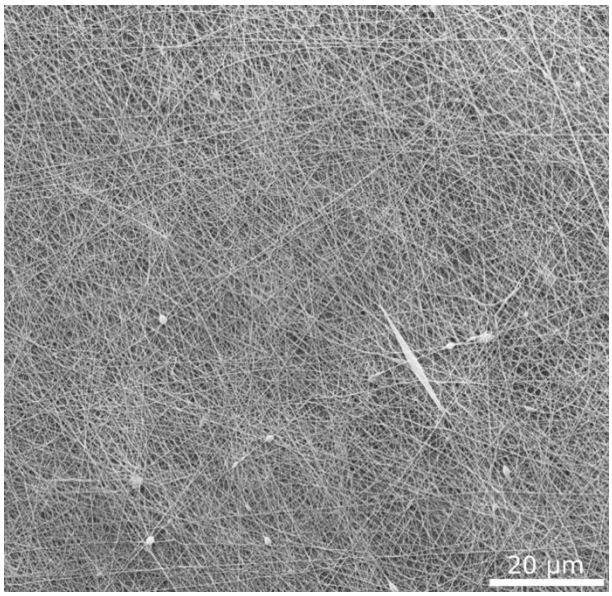

Figure 5: Scanning electron micrograph of electrospun nanofibers. One can see the random orientation of the individual fibers forming a kind of mesh.

The peel-off-force, i.e. the force per unit length of the peeling edge necessary to separate the non-woven from the surface, was measured for the LIPSS-covered samples and for polished surfaces, i.e. flat samples as control. In Figure 6 the peel-off force measurement is exemplified for the polished (Figure 6(a) and 6(b)) and laser-structured (Figure 6(c) and 6(d)) steel samples. The applied weights and hence the normal forces are equal in Figure 6(a) and 6(c) (F_{peel} = 0.54 N) and in Figure 6(b) and 6(d) (F_{peel} = 0.74 N), respectively. The cone diameter *d* of the nanofiber-layer on the LIPSS-covered samples is larger than on the polished samples, which indicates that the peel-off force for the laser-structured samples is lower than for the polished samples.

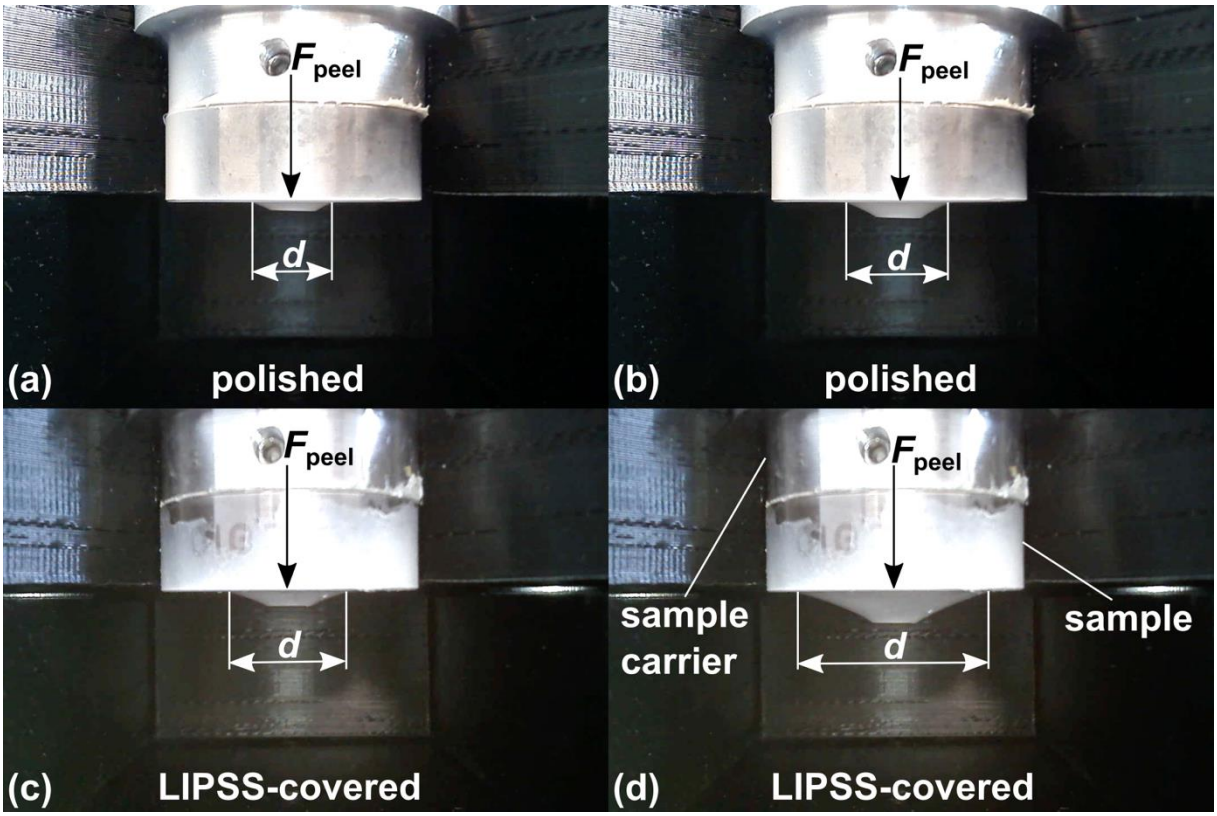

Figure 6: Peel-off force measurement of polished (a, b) and LIPSS-covered (c, d) steel samples. The applied weights and hence the normal forces are equal in (a) and (c) (F_{peel} = 0.54 N) and in (b) and (d) (F_{peel} = 0.74 N), respectively. One can see that the cone diameter *d* at equal applied forces is larger on the LIPSS-covered samples than on the polished samples, which indicates that a peel-off force per unit length is smaller for the laser-structured samples.

Four different sample classes, i.e. titanium (Ti)-alloy polished, Ti-alloy LIPSS-covered, steel polished and steel LIPSS-covered, with two identical samples each were investigated like shown in Figure 6. For every sample class n = 5 different measurements with different weights were performed and the mean values and the standard deviation were calculated for every sample class. Between the measurements the samples were cleaned with 80% ethanol The measured values of

the peel-off forces per unit length needed for the LIPSS-covered titanium-alloy and steel samples are listed in Table 1 and graphically shown as bar plot in Figure 7.

Table 1: Peel-off force per unit length measurement results for all samples in N/m.

Measurement number n	**Ti-alloy polished (N/m)**	**Ti-alloy LIPSS (N/m)**	**Steel polished (N/m)**	**Steel LIPSS (N/m)**
1	3.93	2.50	23.68	6.48
2	3.88	1.52	23.85	6.98
3	4.14	3.54	21.61	6.61
4	8.06	4.16	23.59	14.92
5	10.01	4.31	23.04	12.87
Mean value	6.00	3.21	23.15	9.57
Standard deviation	2.55	1.06	0.82	3.59

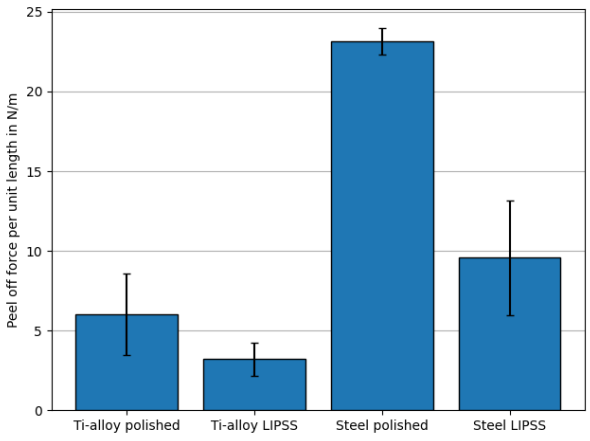

Figure 7: Peel-off force per unit length measurement results from Table 1 (mean values) visualized as bar plot. The error bars denote the standard deviations. Mean peel-off force per unit length is lower for the LIPSS-covered samples than for the polished ones for both steel and titanium-alloy surfaces, albeit to different degrees.

According to Table 1 the mean peel-off forces per unit length were 3 N/m for the LIPSS-covered titanium-alloy and 10 N/m for the LIPSS-covered steel samples and thus lower than for the corresponding polished surfaces (6 N/m for titanium-alloy and 23 N/m for steel). Thus, for both metals (Ti-alloy and steel), the LIPSS reduce the adhesion forces by approximately 50% compared to the polished surface finish.

Additionally, due to the lower peel-off force on the laser-structured samples, no fibers can be found after testing on the laser structured surfaces, whereas on the polished surfaces a layer of fibers remains (OM and SEM). This is shown exemplary for the titanium-alloy samples in Figure 8. Thus, the force measured for peel-off from the polished surface is not the force needed to detach the fibers from the surface, but to tear a superficial fiber layer from the rest of the non-woven.

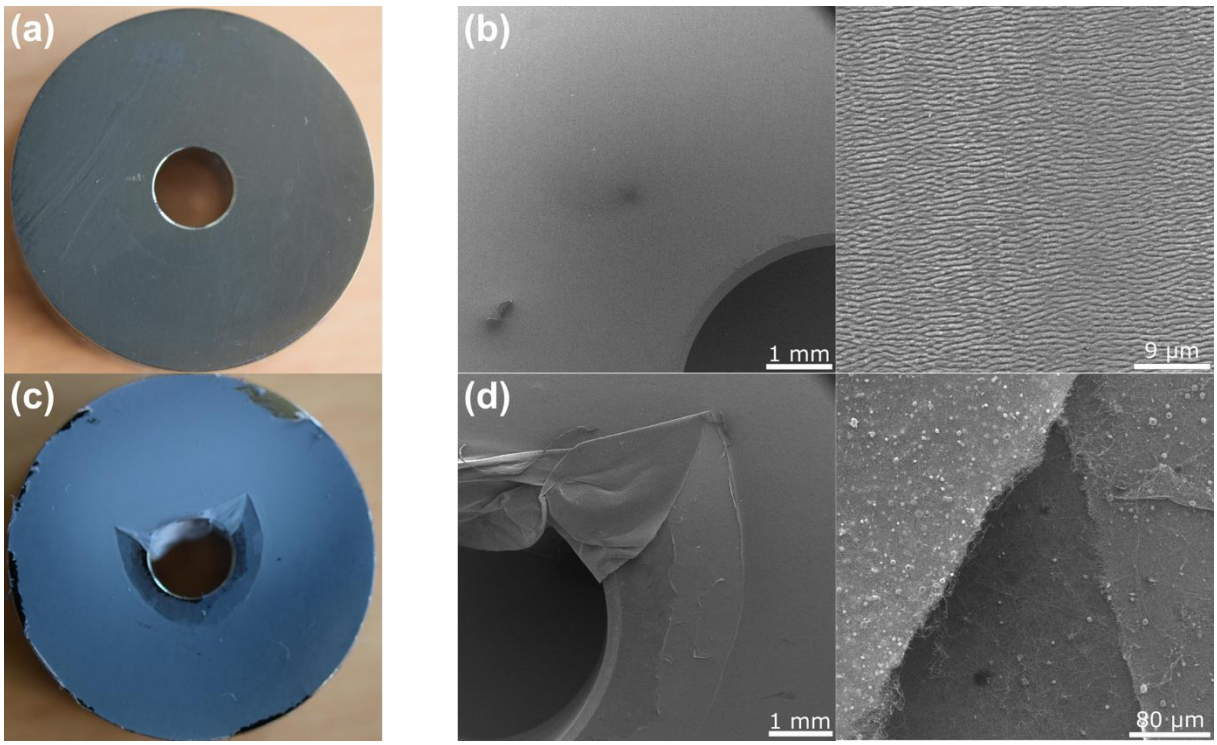

Figure 8: Laser-structured (LIPSS-covered) and polished titanium-alloy surfaces after peel-off of an electrospun non-woven. While the nanofibers could be removed entirely

from the LIPSS (a, b), a film of nanofibers remains on the polished surface (c, d). This can be seen macroscopically (left) as well as in the SEM micrographs (right).

Conclusions

Mimicking the principle of nanostructures on the calamistrum of cribellate spiders, we were able to define an upscaled surface nanostructure with reduced adhesion force towards technical electro spun fibers. The biomimetic surface can be produced on metals by means of ultrashort pulse laser processing of self-organized laser-induced periodic surface structures, so-called laser-induced periodic surface structure (LIPSS). For the technically relevant materials steel and titanium-alloy, the presence of LIPSS reduced the peel-off forces by approximately 50% in both cases. Even more importantly, in contrast to the polished reference surface no nanofibers remained at the LIPSS-covered surfaces.

In this work, only one fiber type was investigated, but in principle these surface structures can be adapted to the requirements for different fiber types, i.e. different diameters and elastic moduli, and thus to different bending stiffness within technical limits. Such non-adhesiveness is beneficial for tools or parts of tools used in the production of nanofibers. A reduced adhesion of non-woven would not only help prevent residues of non-woven on tools used in the production, but will also reduce the chance of tearing or generally damaging the non-woven at separation from a target or a tool. As one can imagine, even small damages of the non-woven during production could lead to severe problems in the application. Refinement and consequent application of the theoretical model described here might help to further optimize the surface structure and/or to find even better structures to make nanofiber non-woven easier to handle and allow for a broader field of applications.

Experimental

Sample materials

Grade-5 titanium-alloy Ti6Al4V was purchased from Schumacher Titan GmbH (Solingen, Germany) as rods of 25 mm diameter. The rods were reduced to 24 mm diameter and cut into ~8 mm thick slabs. Circular slabs of hardened 100Cr6 steel (24 mm diameter, 8 mm thickness) were purchased from Optimol Instruments Prüftechnik GmbH (Munich, Germany). The top surfaces of the samples were mechanically polished resulting in a mirror-like surface finish with an average roughness R_a < 15 nm.

Laser processing

The laser processing was performed using an ultrashort pulse laser (TruMicro 5050 femto edition, TRUMPF, Ditzingen, Germany) with a pulse duration of ~925 fs and a wavelength of 1030 nm, operated at 100 kHz pulse repetition rate. A galvanometer laser scanner (hurrySCAN II 14, SCANLAB GmbH, Puchheim, Germany), equipped with a f-theta lens of 160 mm focal length allowed to scan the focused laser beam across the sample surface. The angle of incidence of the laser beam onto the sample surface was ~0°. The relative position of the sample to the scanner optics was adjusted to place the sample surface in the focal plane of the f-theta lens. At the sample surface, the focal diameter ($1/e^2$) of the Gaussian laser beam was determined by the D^2-method [29] as $2w_0$ = 35.5 µm. The samples were processed at optimized incident peak fluences of ϕ_0 = 0.35 J/cm^2 for Ti6Al4V, and 0.54 J/cm^2 for 100Cr6 and AlMg3, while employing a meandering line-wise processing at a constant scan velocity of v_x = 700 mm/s and an inter-line separation of Δ = 5 µm. The linear laser beam polarization was kept parallel to the scan direction. Immediately after laser processing,

the samples were cleaned for 5 min in acetone in an ultrasonic bath and stored in a desiccator.

Figure 9 provides points towards the presence of the LIPSS at the entire top-surface of the laser-processed Ti6Al4V sample through structural color effects, i.e., optical diffraction of the ambient light at the sub-micrometric grating-like LIPSS. High-resolution optical microscopy (OM) confirmed the presence of LSFL-LIPSS with average spatial periods Λ between 700 and 800 nm (data not shown here). A 5 mm borehole was mechanically drilled through the laser-processed disks prior to the adhesion measurements.

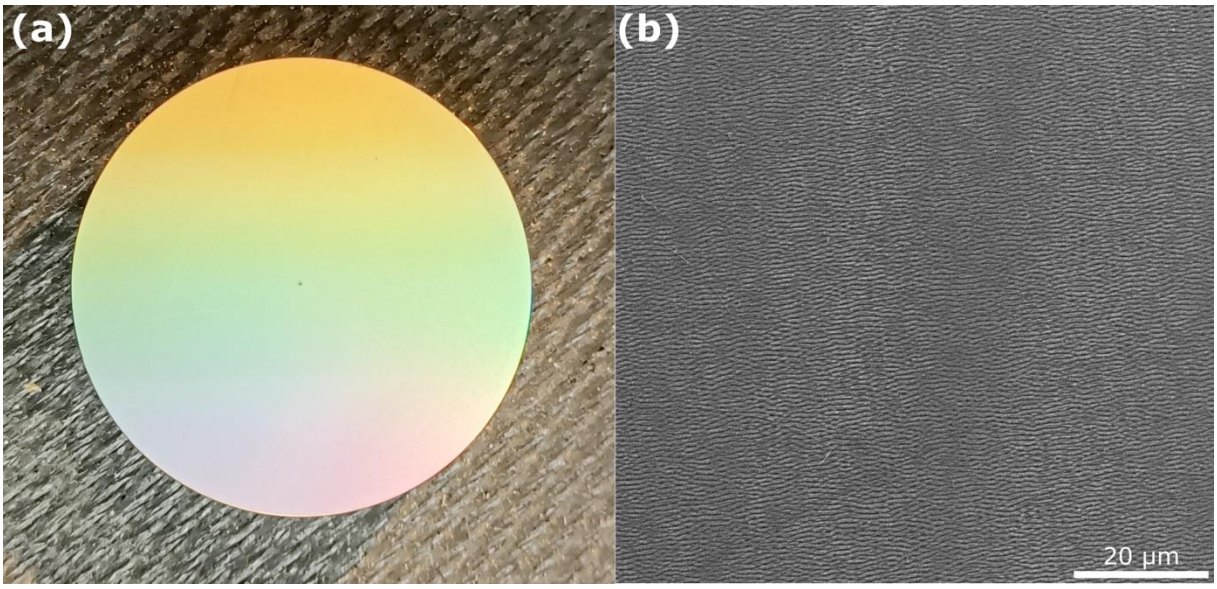

Figure 9: (a) Photograph of a laser structured titanium-alloy sample after ultrafast laser processing. The colorful appearance arises from optical diffraction of the ambient natural light at the grating-like LIPSS-covered surface topography (structural colors). (b) Scanning electron micrograph of the LIPSS-covered titanium-alloy surface.

Electrospinning

The electrospinning process was performed using a custom-made setup (Figure 10). The liquid PA-6 solution consisting of 6 g PA-6 polymer, 15 g formic acid and 29 g acetic acid was mixed at 80°C for about 90 minutes. The dope solution was delivered

to the blunt needle tip (ID 0.6 mm) via a Teflon tube from a 20 mL glass syringe (Dosys Model 155, Scorex Isba SA, Ecublens, Switzerland) using a syringe pump (Perfusor fm, B. Braun, Melsungen, Germany) at a set flow rate of 0.2 mL/h (Figure 10(a)). The sample fixed on an aluminum sample carrier was placed about 5 cm right under the needle. The positive electrode of a high voltage generator (HCP 35 – 35 000, FuG Elektronik GmbH, Schechen, Germany) was clamped onto the needle and the ground electrode was clamped onto the aluminum sample carrier (Figure 10(b)). The corresponding voltage was set to 22 – 23 kV. During the electrospinning process the sample was rotated by hand to achieve a uniform distribution of the nanofibers across the whole sample surface. Figure 10(c) shows a spun sample after the electrospinning process, one can see, that the surface is fully covered with a thin mesh layer of nanofibers, i.e. the non-woven.

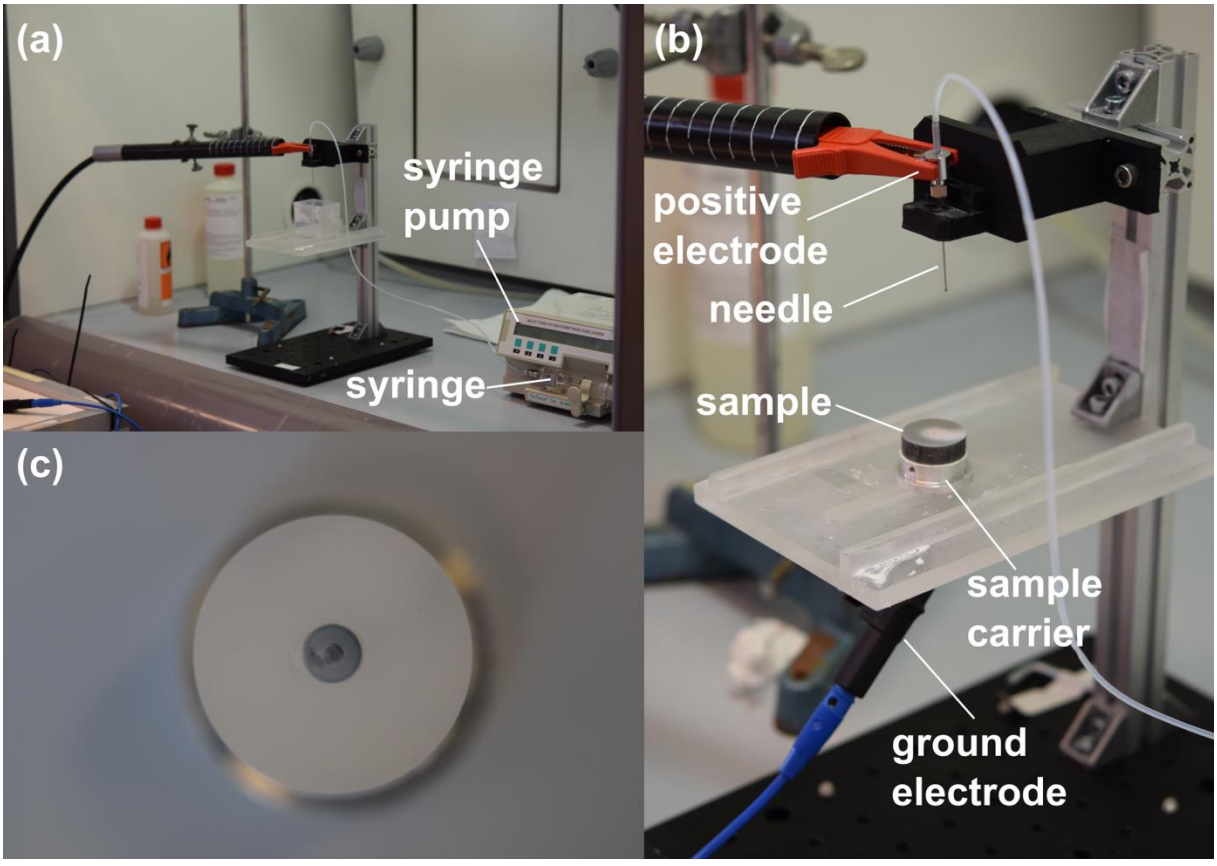

Figure 10: (a) Photography of the setup for the electrospinning process. (b) Close-up view of the electrospinning setup while spinning on a sample. (c) Top-view of the spun

sample after electrospinning, the surface is fully covered with a thin mesh layer of nanofibers (non-woven).

Adhesion measurements

In order to quantify the adhesion of electrospun non-woven, a new peel-off test had to be established. Existing peel-off tests are typically used for rather large samples; thus, the edge effects can be neglected. These effects become dominant when the width of the peeled homogeneous surface becomes small. In order to only peel the non-woven from the interacting homogeneous surface and not from the sample edges (where unpredictable physical effects take place) the following adhesion test setup shown in Figure 11 was built.

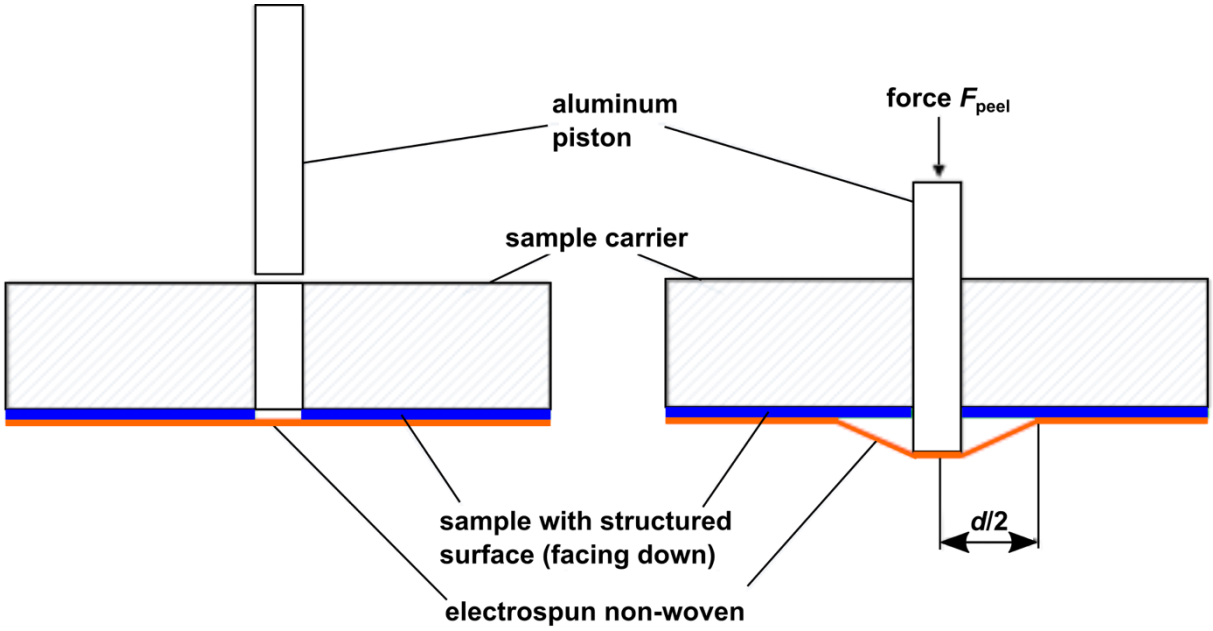

Figure 11: Measurement principle of the newly established peel-off test avoiding edge effects. Blue: laser-structured surface; Orange: Electrospun non-woven. Left: An aluminum piston is put into a 5 mm hole drilled into the sample carrier and the sample. Right: Defined forces F_{peel} are applied onto the aluminum piston by adding defined weights. When exceeding a critical threshold value, the peel-off forces remove the non-

woven from the sample surface, leading to the formation of a cone-like envelope with diameter *d*.

The principle depicted in Figure 11 works as follows. The sample with a surface under investigation is mounted onto a sample carrier. Through this sample and the sample carrier a hole (diameter of 5 mm) is drilled. The hole is then filled with an aluminum piston that is fixed by a screw to form a straight surface. Then the non-woven is spun onto the sample by means of electrospinning. After polymerization of the deposited non-woven, the sample carrier is mounted into a holder and the fixation of the screw is removed. Then defined forces are applied onto the piston by adding weights on it. The non-woven has only negligible bending stiffness macroscopically and, thus, the piston-induced force can only act longitudinal in the non-woven. This force is split vectorial at the point of contact in a vertical peel off force and a local horizontal shear force. Due to the rotational symmetry the total horizontal forces cancel out. When exceeding a critical threshold value, the peel-off forces remove the non-woven from the sample surface, leading to the formation of a cone-like envelope. Thus, the diameter *d* of the cone increases initially until eventually a force equilibrium occurs. This is due to the fact that the total peel-off force depends on the length *c* of the peeling edge. In our case this is

$$F_{peel} = p \cdot c = p \cdot d \cdot \pi. \tag{27}$$

Here, *p* is the peel off force per unit length which is a measure for the adhesion of the non-woven to the surface under investigation. Thus, by optically measuring the diameter *d* of the cone, the peel-off force per unit length can be determined from the known force F_{peel}. The method was tested using siliconized paper and other materials

which were also tested by a commercially available peel-off-meter. Both measurements were found to be in good agreement.

Measurement of the calamistral nanoripples

Amaurobius similis (Blackwall, 1861) and *Uloborus plumipes* (Lucas, 1846) were captured in Aachen, Germany, and kept in the laboratory before being frozen at -20° C. *Jamberoo johnnoblei* (Gray & Smith, 2008) was captured in the wild at Mt. Wilson (Australia) and kept in the laboratory before preserving the species in 70% ethanol. In 70% ethanol preserved specimen of *Hickmania troglodytes* (Higgins & Petterd, 1883) were kindly provided by the Australian Museum (Sydney, Australia). The fourth leg, bearing the calamistrum, was removed from the ethanol-preserved specimen, dried in an ascending ethanol series, which was finally substituted by hexamethyldisilazane. After evaporation, specimen were gold sputtered (Hummer Technics Inc., Alexandria, USA; 7-10 mA, 5 min) and studied with the SEM (525 M, Philips AG, Amsterdam, The Netherlands). Legs of *U. plumipes* were air-dried and otherwise prepared the same way for SEM analysis. Measurements were performed with ImageJ's FIJI software [30].

Legs of *A. similis* were air-dried and gold-sputtered (S150B, Edwards). The metatarsi were examined using focused ion beam scanning electron microscope (FIB-SEM) tomography (Strata 400 STEM, FEI Company, Oregon, USA) at the Central Facility for Electron Microscopy at the RWTH Aachen University. Measurements were performed using the accompanying software (xT Microscope Control).

For all spiders, we measured the peak-to-peak amplitude of the nanoripples covering the calamistrum at the region of interest. In addition, FIB tomography was used to measure the depth of structure in *A. similis*.

Supporting Information

Supporting Information File 1:

File Name: Supplement to Laser-processed antiadhesive bionic combs for handling of nanofibers inspired by nanostructures on the legs of cribellate spiders

File Format: Microsoft Word

Title: Supplement: Laser-processed antiadhesive bionic combs for handling of nanofibers inspired by nanostructures on the legs of cribellate spiders

Acknowledgements

The authors would like to thank K. Zieger and C. Opitz (BAM division 9.5) for polishing the metal samples as well as K. Kistermann (GFE Aachen) for his active support at the FIB-SEM.

Funding

This work was supported by the European Union's Horizon 2020 research and innovation program within the project "BioCombs4Nanofibers" (Grant Agreement No. 862016, http://biocombs4nanofibers.eu). ACJ was funded by the Deutsche Forschungsgemeinschaft (JO1464/1-1).

References

1. Wu, Y. B.; Wang, L.; Guo, B. L.; Ma, P. X. *ACS Nano* **2017**, 11 (6), 5646−5659. doi.org/10.1021/acsnano.7b01062

2. Ramakrishna, S.; Fujihara, K.; Teo, W.-E.; Yong, T.; Ma, Z.; Ramaseshan, R. *Mater. Today* **2006**, 9 (3), 40 − 50. doi.org/10.1016/S1369-7021(06)71389-X

3. Akampumuza, O.; Gao, H. C.; Zhang, H. N.; Wu, D. Q.; Qin, X. H. *Macromol. Mater. Eng.* **2018**, 303 (1), No. 1700269. doi.org/10.1002/mame.201700269

4. Costa-Almeida, R.; Gasperini, L.; Borges, J.; Babo, P. S.; Rodrigues, M. T.; Mano, J. F.; Reis, R. L.; Gomes, M. E. *ACS Biomater. Sci. Eng.* **2017**, 3 (7), 1322 − 1331. doi.org/10.1021/acsbiomaterials.6b00331

5. Vasita, R.; Katti, D. S. *Int. J. Nanomedicine* **2006**, 1(1), 15 – 30. doi.org/10.2147/nano.2006.1.1.15

6. Zhang, B.; Kang, F.; Tarascon, J. M.; Kim, J. K. *Progress in Materials Science* **2016**, 76, 319 – 380. doi.org/10.1016/j.pmatsci.2015.08.002

7. Wang, X.; Drew, C.; Lee, S. H.; Senecal, K. J.; Kumar, J.; Samuelson, L. A. *Nano Letters* **2002**, 2(11), 1273 – 1275. doi.org/10.1021/nl020216u

8. SalehHudin, H. S.; Mohamad, E. N.; Mahadi, W. N. L.; Muhammad Afifi, A. *Materials and Manufacturing Processes* **2018**, 33(5), 479 – 498. doi.org/10.1080/10426914.2017.1388523

9. Adrian Parsegian, V. *Van der Waals forces: A handbook for biologists, chemists, engineers, and physicists*; Cambridge Univ. Press: New York, USA, 2005. doi.org/10.1017/CBO9780511614606

10. Joel, A.-C.; Meyer, M.; Heitz, J.; Heiss, A.; Park, D.; Adamova, H.; Baumgartner, W. *ACS Applied Nano Materials* **2020**, 3(4), 3395 – 3401. doi.org/10.1021/acsanm.0c00130

11. Joel, A.-C.; Kappel, P.; Adamova, H.; Baumgartner, W.; Scholz, I. *Arthropod Struct. Dev.* **2015**, 44 (6), 568 − 573. doi.org/10.1016/j.asd.2015.07.003

12. Michalik, P.; Piorkowski, D.; Blackledge, T. A.; Ramírez, M. J. *Sci. Rep.* **2019**, 9(1), No. 9092. doi.org/10.1038/s41598-019-45552-x

13. Bott, R. A.; Baumgartner, W.; Bräunig, P.; Menzel, F.; Joel, A.-C. *Proc. R. Soc. London* **2017**, 284 (1855), No. 20170363. doi.org/10.1098/rspb.2017.0363

14. Hawthorn, A. C.; Opell, B. D. *J. Exp. Biol.* **2003**, 206, 3905 - 3911. doi.org/10.1242/jeb.00618

15. Piorkowski, D.; Blamires, S. J.; Doran, N. E.; Liao, C.-P.; Wu, C.-L.; Tso, I.-M. *J Zool* **2018,** 304(2), 81 – 89. doi.org/10.1111/jzo.12507

16. Doran, N.; Kiernan, K.; Swain, R; Richardson, A. M. M. *Journal of Insect Conservation* **1999**, 3(4), 257 – 262. doi.org/10.1023/A:1009677531343

17. Joel, A.-C.; Habedank, A.; Hausen, J.; Mey, J. *Zoology* **2017**, 121, 10 - 17. doi.org/10.1016/j.zool.2016.12.002

18. Gray, M. R.; Smith, H. M. *Rec. Aust. Mus* **2008**, 60(1), 13 – 44. doi.org/10.3853/j.0067-1975.60.2008.1493

19. World Spider Catalog, 2022. World Spider Catalog. Version 23.0. Natural History Museum Bern. http://wsc.nmbe.ch/ (accessed January 21, 2022).

20. Barthlott, W.; Neinhuis, C. The Lotus-effect: A paradigm for the use of a natural design for technical application. In *Meeting of the Botanical Society of America*, Maryland, USA, August 2 - 6, 1998; Am. J. Bot. 85 (6), 6.

21. Barthlott, W.; Neinhuis, C. *Planta* **1997**, 202(1), 1 - 8. doi.org/10.1007/s004250050096

22. Koch, K.; Bohn, H. F.; Barthlott, W. *Langmuir* **2009**, 25 (24), 14116 - 14120. doi.org/10.1021/la9017322

23. Koch, K.; Bhushan, B.; Barthlott, W. Functional plant surfaces, smart materials. In *Handbook of Nanotechnology*; Bhushan, B., Ed.; Springer Heidelberg London New York, 2010; 3rd Ed., p. 1961: 1399 - 1436. doi.org/10.1007/978-3-642-02525-9

24. Bonse, J.; Krüger, J.; Höhm, S.; Rosenfeld, A. *Journal of Laser Applications* **2012,** 24, No. 042006. doi.org/10.2351/1.4712658

25. Gross, D.; Hauger, W.; Schröder, J.; Wall, W. Balkenbiegung. In *Technische Mechanik 2*; Springer Lehrbuch; Springer Vieweg, Berlin, Heidelberg, 2014; Vol. 12, pp. 87 - 173. doi.org/10.1007/978-3-642-40966-0_4

26. Opell, B. D.; Bond, J. E. *Evolutionary Ecology Research* **2001**, 3 (5), 507 - 519.

27. Preliminary datasheet of PA-6, February 12, 2019. https://akro-plastic.com/productfilter/details/2315/ (accessed March 25, 2022).

28. Bonse, J.; Kirner, S. V.; Krüger, J. Laser-Induced Periodic Surface Structures (LIPSS). In *Handbook of Laser Micro- and Nano-Engineering*; Sugioka, K., Ed; Springer Nature Switzerland AG: Cham, Switzerland, 2021, Volume 2, Part IV pp 879-936. 2021. doi.org/10.1007/978-3-030-63647-0_17

29. Liu, J. M. *Opt. Lett.* **1982**, 7(5), 196 – 198. doi.org/10.1364/OL.7.000196

30. Schneider, C. A.; Rasband, W. S.; Eliceiri, K. W. *Nature Methods* **2012**, 9(7), 671 – 675. doi:10.1038/nmeth.2089